Available online at www.sciencedirect.com

SciVerse ScienceDirect

Ceramics International 38 (2012) 3047–3055

CERAMICS INTERNATIONAL

www.elsevier.com/locate/ceramint

Complex impedance studies of low temperature synthesized fine grain PZT/CeO_2 nanocomposites

Puja Goel *, N. Vijayan, Ashok M. Biradar

National Physical Laboratory, Dr. K.S. Krishnan Marg, New Delhi 110012, India

Received 13 October 2011; received in revised form 1 December 2011; accepted 1 December 2011
Available online 8 December 2011

Abstract

Fine grain nanocomposites of $(100-x)$ $PbZr_{0.52}Ti_{0.48}O_3-(x)$ CeO_2 with $x=0.5$, 1 and 2 wt%, were prepared and characterized for structural and microstructural changes. Addition of ceria nanoparticles resulted into a fine grain microstructure with average grain size ranging from 600 nm to 440 nm and a significant decrease in sintering temperature (~200 °C). Size distribution profile, as analyzed by lognormal distribution function suggests a very narrow size distribution. X-ray diffraction analyses of sintered samples reveal that fine grain PZT/CeO_2 nanocomposite could retain distorted tetragonal structure even with grain size as low as 440 nm. Further, complex impedance spectroscopy studies were performed to illustrate the electrical properties of bulk and grain boundary phases in fine grain ceramics. Two electrical processes in the impedance spectra at temperatures above 350 °C were attributed to bulk and grain boundary phase. Magnitude of grain boundary capacitance and corresponding transition was found to be strongly dependent on grain size of the system. Both bulk and grain boundary relaxation processes follows Arrhenius law.

Keywords: A. Sol–gel; B. Nanocomposites; C. Ferroelectric; D. Complex impedance

1. Introduction

Ferroelectric oxide ceramic lead zircconate titanate (PZT) has drawn substantial interest for variety of technological applications [1–3]. For example, in dynamic random access memories, high dielectric permittivity of ferroelectric materials has been considered, high quadratic and linear electro-optic coefficients are of major interest for electro-optic applications. The true ferroelectricity, i.e. the hysteretic behavior of electrical polarization in presence of external electric field, makes them promising candidate for non-volatile data storage. However, for cutting down the size of the ferroelectric based memory element, there are lots of issues which need to be considered. One of the major facts which is important from both technological as well as fundamental point of view is the size effect on ferroelectricity. As the grain size reaches to submicron regime, there is enormous change in lattice structure, phase transition temperature and ferroelectric polarization. Consequently, the origin of grain size effect in nanocrystalline ferroelectrics, ferroelectric nanoparticles and thin films has been a subject of lot of theoretical and experimental research [4–6]. Recently, many people have also taken into account the incorporation of small amount of secondary phase nanoparticles in to PZT. In these types of ceramic–nanoparticles systems, known as nanocomposites, microstructure is substantially modified which in turn resulted into a change in lattice structure and mechanical properties [7–9]. As far as microstructure is considered, none of the secondary phase nanoparticles into PZT could lead to a fine grain microstructure.

In current study fine grain microstructure could be achieved by small addition of ceria nanoparticles into sol–gel derived PZT at a much lowered sintering temperature. Resulting changes in the phase structure and extent of tetragonality is studied with respect to changes in microstructure. Impedance data has been presented in a variety of forms to explicate the temperature-frequency dependent bulk and grain boundary responses associated with the microstructural feature of the nanocomposites.

* Corresponding author.
E-mail address: pujagoel@gmail.com (P. Goel).

0272-8842/$36.00
doi:10.1016/j.ceramint.2011.12.002

2. Experiment

The nanocomposites of $(100 - x)$ $Pb(Zr_{0.52}Ti_{0.48})O_3/xCeO_2$ ($x = 0.5$, 1, 2 wt%) were prepared by making use of sol–gel technique. Lead acetate trihydrate $[Pb(CH_3COO)_2{\cdot}3H_2O]$, zirconyl acetyl acetonate $[(C_5H_7O_2)_4Zr]$, titanium isopropoxide $[Ti[(CH_3)_2CHO]_4]$ (all from Sigma Aldrich, 99% purity) were taken in a molar ratio according to $Pb(Zr_{0.52}Ti_{0.48})O_3$. Synthesis details remain similar as followed earlier [10]. Calcination of powder was carried out at 600 °C for 6 h and amorphous powder converts into perovskite phase PZT. For the preparation of nanocomposites, CeO_2 nanopowder (Sigma Aldrich, ~25 nm) was added to PZT powder in 0.5, 1, 2 wt% ratio followed by 5 h grinding in agate mortar. These powders were pressed in the form of pellets of approximately 10 mm diameter at a pressure of 6×10^6 N/m^2 by using Hydraulic Press. Polyvinyl alcohol (PVA) was used as a binder during pellet preparation which aids the compaction process and will be burnt out by 30 min of heating at 500 °C during sintering. Optimum sintering temperature for nanocomposites was found to be 1000 °C and for pure PZT it was 1200 °C. Pellets were placed in recrystallized alumina crucible and sintered for 2 h duration in $PbZrO_3$ atmosphere at aforesaid temperatures. Crystal structure and phase identification of sintered pellets was carried out by X-ray diffractometer (XRD, Brueker D8 Advance) using Cu Kα radiation ($\lambda = 1.5414$ Å), Lattice parameters were also calculated and refined using least square method. Microstructure was analyzed using scanning electron microscope (SEM, LEO 440) coupled with energy dispersive spectroscopy (Oxford link ISIS 300). Complex impedance parameters at different temperatures were measured by an impedance analyzer (PSM1735-Numetriq) in the frequency range 100 Hz to 4 MHz.

3. Results and discussion

3.1. Microstructure

Surface morphology, grain size and size distribution on sintered ceramics were analyzed by scanning electron microscopy (SEM). Flat surfaces of all the sintered bodies are shown in Fig. 1. Fine circular grains with clear grain

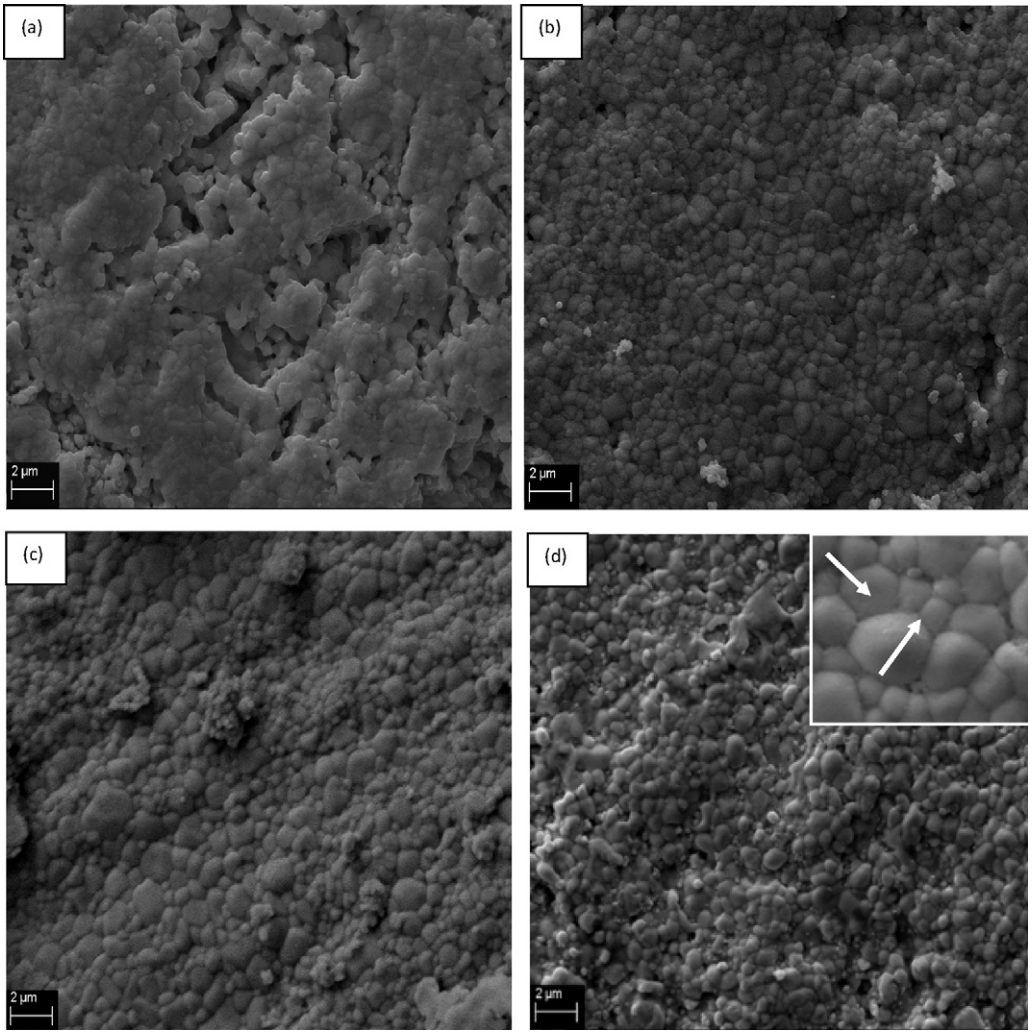

Fig. 1. SEM micrographs of flat surfaces of sintered samples of $(100 - x)$PZT/xCeO$_2$ (a) $x = 0.0$ (b) $x = 0.5$ (c) $x = 1$ and (d) $x = 2$ (inset of (d) indicates the traces (marked by arrows) of nanoparticles in $(100 - x)$ PZT/xCeO$_2$ for $x = 2$.

boundaries are observed with all nanocomposites even without any surface polishing and chemical etching. Grain size decreases with increasing ceria NP concentration up to 2 wt% and lies in a range of 600–440 nm. Reduction in grain size might be due to so called inhibition effect which restrains the grain growth in presence of secondary phase nanoparticles. A 200 °C decrease in sintering temperature also indicates that the ceria addition promotes the densification while restricting the grain growth in nanocomposite formation.

A close look at the microstructure in higher resolution micrographs (inset Fig. 1(d)) evidenced some traces of nanoparticles over the grain surface in highest ceria NP weight ratio (i.e. 2 wt%). Density of all sintered Nanocomposites was found to be comparable/slightly higher to PZT sample even at a lower sintering temperature. Therefore, it is noticeable that ceria nanoparticles are effective in suppressing grain growth without losing the densification of PZT.

Fig. 2 shows the grain-size distribution profile in nanocomposites represented by corresponding histograms taking into account 250 grains. The solid line in Fig. 2(a–c) represents the best curve fit of the particle-size histogram using the standard approach and can be well described by the lognormal distribution function

$$y = y_0 + \frac{A}{w \times x\sqrt{2\pi}} \exp\left(-\frac{(\ln(x/x_c))^2}{2 \times w^2}\right),$$

where w is standard deviation and x_c represents mean grain size. The width of distribution or the standard deviation becomes narrower with increasing NP weight ratio (details are given in Table 1). It is therefore believed that minute incorporation of ceria NP not only controlled the grain growth but resulted into a fine grain size and size distribution by capping the PZT grains. Energy dispersive X-ray analysis (EDAX) at the grain boundary area ruled out the possibility of the formation of secondary phases at the grain boundary area up to 1 wt% addition (Fig. 3).

3.2. X-ray diffraction studies

Fig. 4(a) shows the XRD pattern of CeO_2 Nanopowder and the XRD patterns of sintered pellets of $(100 - x)$ PZT/xCeO$_2$ with different x values are shown in Fig. 4(b). Average particle size for ceria nanoparticles estimated from XRD pattern using Scherrer's equation [11] $(P = ((k\lambda)/(\beta_{1/2}\cos\theta)))$, where $k = 0.89$, λ = wavelength of X-ray and $\beta_{1/2}$ is full-width at half maximum intensity (FWHM), is around 25 nm which exactly matches with the size claimed by the manufacturer. In Fig. 4(b), the single and sharp intensity peaks in all nanocomposites indicate the formation of tetragonal perovskite phase without affecting the basic crystal structure of PZT. No peak of ceria was identified in the diffraction patterns of sintered bodies. Just to get an idea of where these secondary phase nanoparticles go in to the system, sintered pellets were crushed and ground into fine powders and XRD patterns were recorded again. These patterns (Fig. 4(c)) clearly reflect the major peaks of ceria along with PZT. It is interesting to note that the intensity ratio of (1 1 1) and (2 0 0) peaks of ceria was

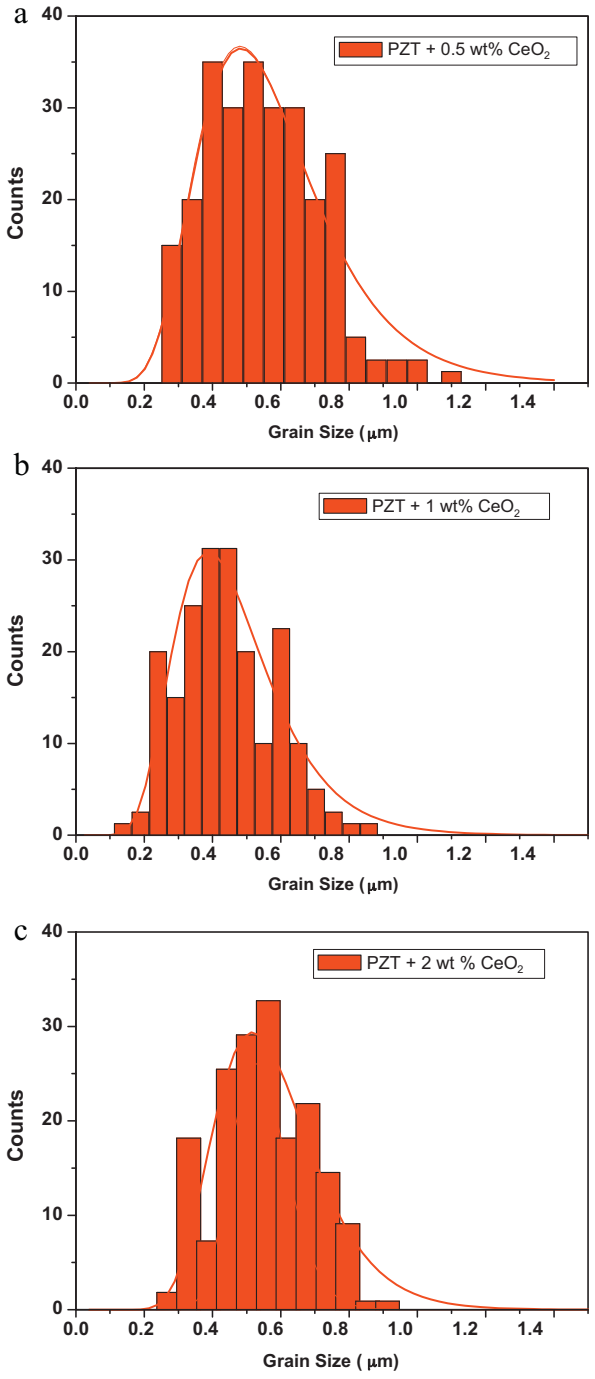

Fig. 2. Grain size distribution histograms for $(100 - x)$PZT/xCeO$_2$ (a) $x = 0.5$ (b) $x = 1$ and (c) $x = 2$.

different in bulk (Fig. 4(a)) and nanocomposites (Fig. 4(c)) which is indicative of the preferred orientation of ceria nanoparticles in nanocomposite formation [12]. It is also evident that there is very less probability of ceria being dissolved into the PZT lattice but it remain either on the grain surface or at grain boundaries in nanocomposite system.

In addition to the above observations, tetragonality and particle size of all the sintered samples have been calculated and their corresponding variation with ceria addition is given in Table 1. Tetragonality is exactly following the particle size

Table 1
Structural parameters, grain size and distribution width for $(100 - x)$PZT/xCeO$_2$ nanocomposites.

Composition	Avg. grain size by linear intercept method (μm)	Mean grain size (x_c) along with width of size distribution w (nm)	Lattice parameters a and c (Å)	Particle size (nm)	Tetragonality (c/a ratio)
$x = 0.0$	1.1	–	$a = 4.0385$ $c = 4.1476$	38	1.027
$x = 0.5$	0.598	0.543 ± 0.356	$a = 4.0232$ $c = 4.1439$	47	1.030
$x = 1$	0.504	0.432 ± 0.245	$a = 4.0220$ $c = 4.1387$	44	1.029
$x = 2$	0.437	0.410 ± 0.150	$a = 4.0333$ $c = 4.1302$	22	1.024

variation in fine grain nanocomposites. It is worth noticing that nanocomposites with $x = 0.5$ and 1 wt% have a higher amount of tetragonality than base PZT (52/48) composition, although their grain sizes lies in submicron regime. However, with 2 wt% ceria addition, tetragonality as well as particle size slightly decreases.

In general, the amount of tetragonality is directly related to the amount of ferroelectricity and stability of ferroelectric phase transition in these ceramic systems. It has been found that as the crystallite size/grain decreases, the tetragonal distortion as well as the amount of ferroelectricity decreases [6–8,13]. Uta Helbig explored the grain size dependence of sol–gel synthesized Nd doped PZT and their results show that the phase boundary is shifted towards higher titanium contents for submicron grain sizes and the peak splitting is slightly less well defined [13]. In addition to that, while going from high grain size to lower size c-axes are significantly compressed and tetragonality also reduced from 1.028 to 1.023 in Nd doped PZT [13]. Reduction of tetragonal distortion and consequently the reduction in Curie temperature are also reported for fine grain BT ceramics ranging from 1200 to 50 nm [14]. In Table 1, calculated lattice parameters (a, c) for all the nanocomposites are presented. With grain size reduction, though the "c" axes are significantly compressed but the corresponding suppression in "a" axes resulted into higher tetragonality with 0.5 and 1 wt% ceria addition. The capping of PZT grains by ceria may induce strain in the lattice and resulted into a higher c/a ratio in 0.5 and 1 wt% CeO$_2$ NP added PZT. With 2 wt% of ceria addition, yet the structure remains tetragonal, c/a ratio is slightly less in comparison to base PZT (52/48) composition.

Since the size effect arising in nanoparticles, ceramics, thin films and composites owed to different electric and elastic boundary conditions, in PZT/CeO$_2$ nanocomposites, ceria nanoparticles are playing a crucial role in modifying the boundary conditions and preserving the tetragonal structure in the submicron regime.

3.3. Complex impedance spectroscopy studies

Temperature-frequency dependent complex impedance spectroscopy (CIS) studies have been carried out in view of its simplicity and importance in describing the electrical processes occurring in a system. In general the data in the complex plane could be represented in any of the four basic formulations. These are complex impedance (Z^*), complex admittance (Y^*), complex permittivity ($\varepsilon_r{}^*$) and complex modulus (M^*) which are inter-related. Since, these nanocomposites have fine grain microstructure; a large concentration of grain boundaries will very likely be contributing to dielectric process occurring in the material. In view of the fact that the relaxation times of bulk and grain boundary process may differ as a consequence of different capacitive components, the complex impedance representation is made use of. In the complex impedance plots of Z' vs. Z'' (Nyquists diagram), depending on the relative values of their relaxation times they may give rise to three semicircular arcs. The classical model to

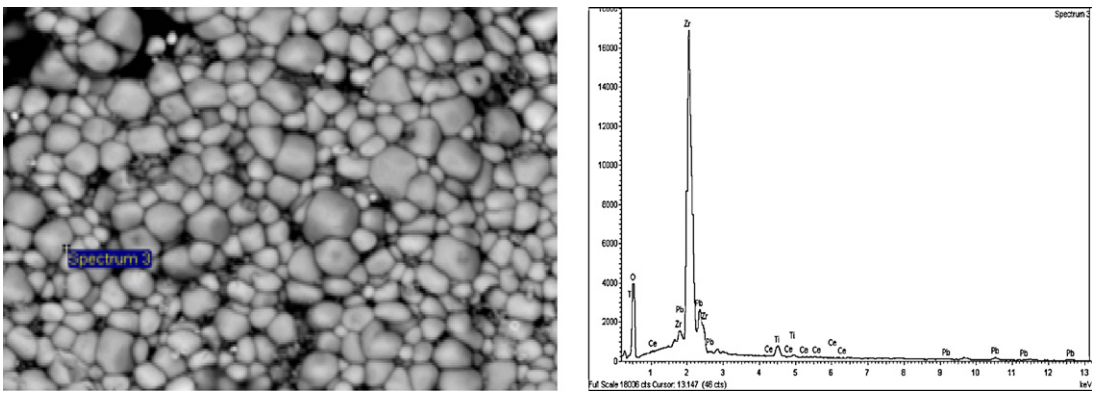

Fig. 3. EDAX spectra of $(100 - x)$ PZT/xCeO$_2$ nanocomposites for $x = 1$ at the grain boundary area.

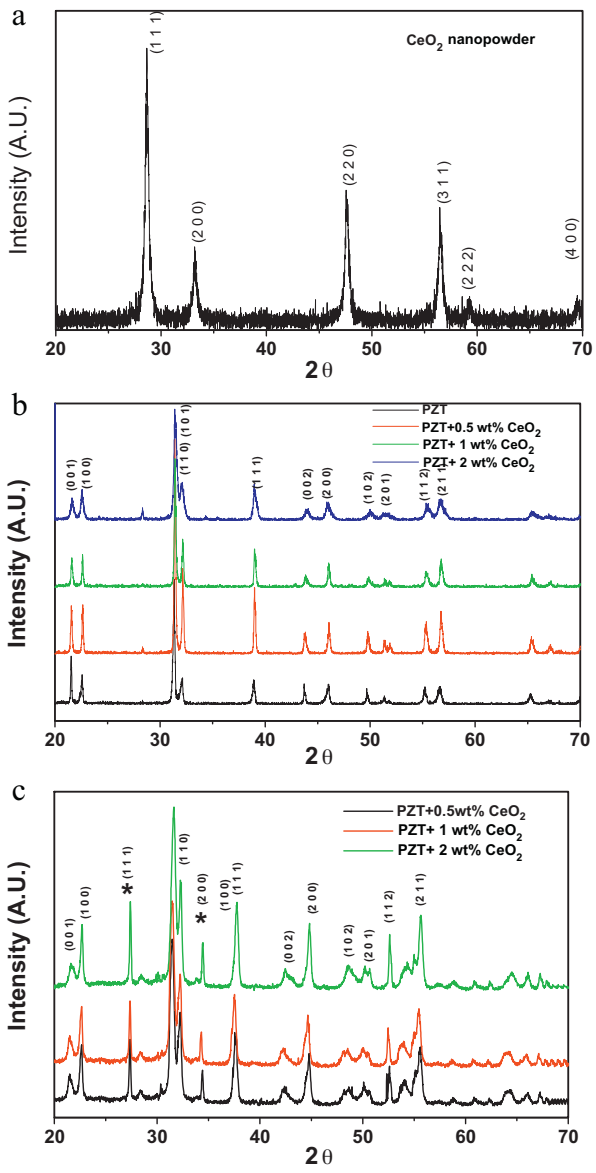

Fig. 4. (a) XRD pattern of CeO_2 nanopowder (b) XRD patterns of sintered pellets of $(100-x)$ PZT/$x$$CeO_2$ nanocomposites (c) XRD patterns of powder (crushed pellets) sample of $(100-x)$ PZT/$x$$CeO_2$ nanocomposites for $x = 0.5$, 1 and 2 (peaks of Ceria are indicated by "*").

describe the impedance behavior is that of Debye and it is written in the form [15]

$$Z^* = Z' - iZ'' \tag{1}$$

$$= \frac{Z_0}{1 + i\omega\tau_0} \tag{2}$$

where, $\tau_0 = (1/\omega_0) = RC$, τ_0 and ω_0 are relaxation time and relaxation frequency respectively. This equation implies a simple electrical circuit of parallel resistance (R) and capacitance (C) which gives rise to a semicircle whose center lies on the real axis in the complex plane (Z' vs. Z'') or a Debye peak in the spectroscopic plots of the imaginary component (Z'' vs. log f).

Fig. 5 shows the Z' vs. Z'' (Nyquist diagram) plots for nanocomposites in 300 °C to 500 °C temperature range. The close inspections of these plots showed that semicircular arc (s) have their centers slightly off the real axis which suggests a small departure from the ideal Debye behavior in nanocomposites. The behavior of such electrical response follows Cole–Cole formalism which is derived by introducing a temperature dependent factor "n" in Debye expression [16]

$$Z = \frac{Z_0}{1 + (i\omega\tau_0)^{1-n}}$$

This relation suggests that the semicircle obtained in complex impedance spectrum has center slightly below the real axis.

At 300 °C, there is only one semicircle like arc which indicates a single electrical process occurring in the nanocomposites. There appear another semicircular arc in the lower frequency side of impedance spectra as soon as the temperature reaches 350 °C. At lower temperatures, ferroelectric grains which are covered with non-ferroelectric ceria phase, remain immobile. However, when the temperature rises, both bulk and grain boundary phases get activated and contribute to the electrical properties of the composite system. Each of these phenomena can be modeled as an equivalent electrical circuit comprising of a series combination of two parallel RC circuits. One RC equivalent is to represent bulk capacitance (C_g) and resistance (R_g) and another is to represent grain boundary capacitance (C_{gb}) and resistance (R_{gb}). Impedance for the equivalent circuit can be expressed as [17]

$$Z^* = Z' - iZ''$$

$$= \frac{1}{R_g^{-1} + i\omega C_g} + \frac{1}{R_{gb}^{-1} + i\omega C_{gb}} \tag{3}$$

where,

$$Z' = \frac{R_g}{1 + (\omega R_g C_g)^2} + \frac{R_{gb}}{1 + (\omega R_{gb} C_{gb})^2} \tag{4}$$

and

$$Z'' = R_g\left[\frac{\omega R_g C_g}{1 + (\omega R_g C_g)^2}\right] + R_{gb}\left[\frac{\omega R_g C_g}{1 + (\omega R_{gb} C_{gb})^2}\right] \tag{5}$$

In general, the peak frequency for grain boundaries is much lower than that for grains due to their large resistance and capacitance compared with those of grains [17–21]. Therefore, in impedance spectra (Fig. 5), we attribute large semicircular arc on high frequency end (lower relaxation time) to the bulk process (grain) and the small arc on lower frequency side to the grain boundary effect. Bulk and grain boundary resistances (R_g, R_{gb}) at different temperatures were obtained from the intercept of the corresponding semicircular arcs on the real Z' axis. Bulk and grain boundary relaxation frequencies (f_g, f_{gb}) have also been extracted from complex impedance plots by applying $\omega = 2\pi f$ (see Table 2) at response peaks of bulk and grain boundaries. Corresponding bulk and grain boundary capaci-

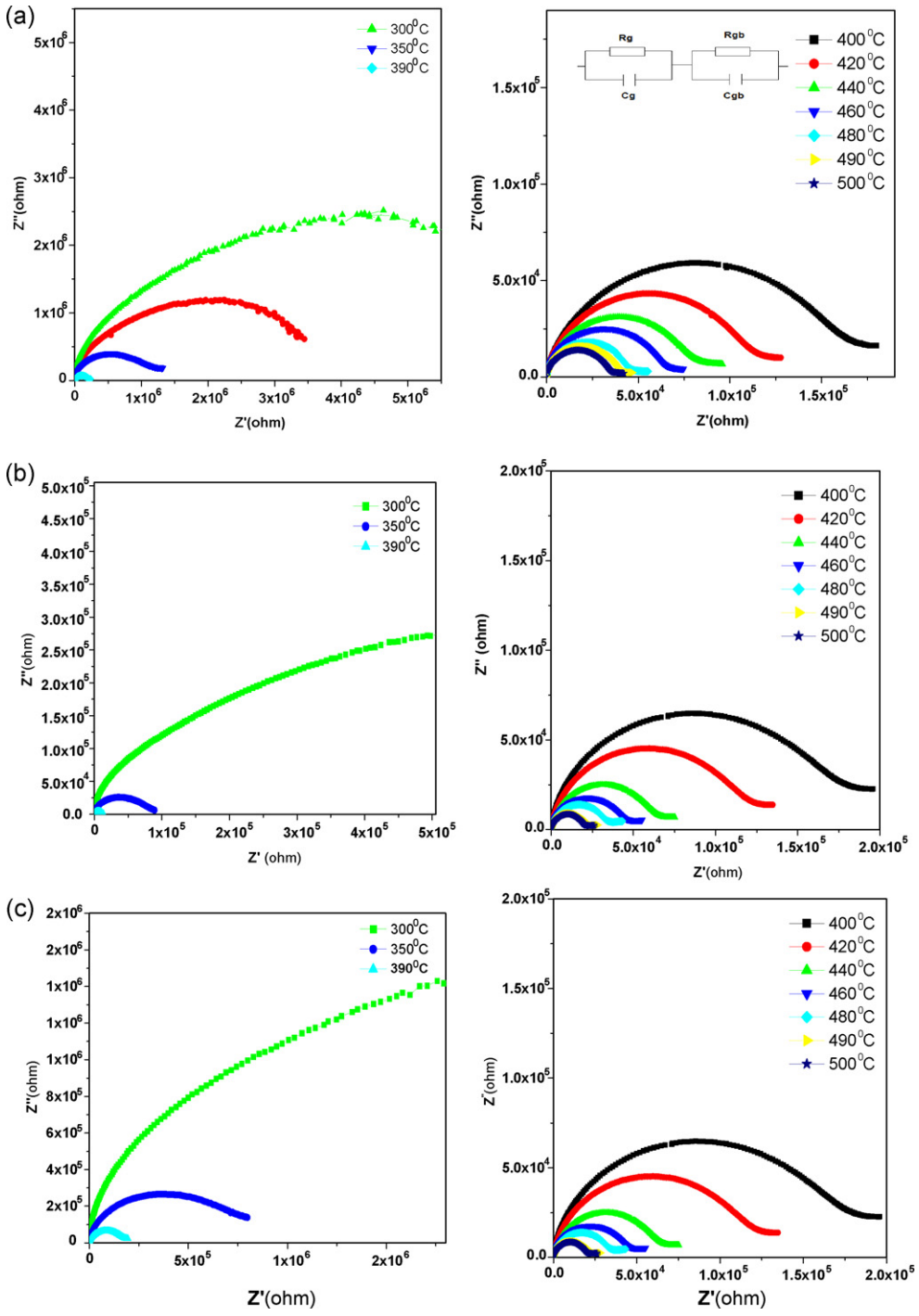

Fig. 5. Cole–Cole plots for $(100 - x)$ PZT/xCeO$_2$ nanocomposites (a) $x = 0.5$, (b) $x = 1$ and (c) $x = 2$ at different temperatures.

tance (C_g, C_{gb}) values were calculated by applying $C_g = 1/2\pi R_g f_g$ and $C_{gb} = 1/2\pi R_{gb} f_{gb}$, respectively. Temperature variation of calculated bulk (C_g) and grain boundary (C_{gb}) capacitance are depicted in Fig. 6(lines are guide to eye only). Magnitude of C_{gb} is several order higher than C_g. Fig. 6 shows that bulk capacitance C_g shows maxima (Curie point) in the measured temperature range and follows the Curie–Weiss behavior above the Curie point. It is also evident from Fig. 6(a–b) that grain boundary capacitance C_{gb} shows maxima in the measured temperature range which overlaps with maxima of C_g indicating a large grain boundary contribution near the Curie point. In 2 wt% ceria addition, these maxima gets well separated and comparatively lower contribution of the grain boundary phase at bulk transition temperature. The temperature of maxima of C_g shifted towards higher temperature with decreasing grain size or increasing ceria weight ratio which might be ascribed to the increase in the concentration of grain boundaries. However, the temperature of maxima C_{gb} does not show a regular trend with grain size reduction which might be due to complex domain formation in fine grain microstructure.

Table 2
Calculated bulk and grain boundary resistances (R_g, R_{gb}) and relaxation frequencies (f_g, f_{gb}) in wide temperature range for $(100-x)$ PZT/xCeO$_2$ nanocomposites.

Temperature (°C)	R_g (MΩ)	R_{gb} (MΩ)	f_g (kHz)	f_{gb} (Hz)	R_g (MΩ)	R_{gb} (MΩ)	f_g (kHz)	f_{gb} (Hz)	R_g (MΩ)	R_{gb} (MΩ)	f_g (kHz)	f_{gb} (Hz)
	$x = 0.5$				$x = 1$				$x = 2$			
350	1.071	0.421	5	135	0.075	0.021	9	119	0.703	0.312	2	119
360	1.070	0.400	9	130	0.043	0.011	16	218	0.483	0.258	3	113
370	1.067	0.389	10	130	0.026	0.006	26	260	0.365	0.158	4	161
380	0.983	0.235	11	125	0.015	0.004	38	323	0.215	0.124	6	176
390	0.211	0.074	12	100	0.176	0.063	6	100	0.160	0.072	7	141
400	0.151	0.055	13	124	1.113	0.033	9	124	0.118	0.039	9	129
420	0.106	0.043	23	193	0.067	0.019	21	192	0.066	0.025	21	168
440	0.077	0.036	52	141	0.045	0.015	38	141	0.047	0.019	35	154
480	0.045	0.012	177	271	0.025	0.008	109	271	0.024	0.011	109	309
490	0.043	0.010	190	304	0.025	0.009	136	321	0.021	0.009	125	296
500	0.039	0.008	205	312	0.023	0.009	142	356	0.020	0.008	132	200
510	0.035	0.007	250	356	0.022	0.0086	160	435	0.018	0.007	150	228
520	0.028	0.005	270	402	0.019	0.0085	180	483	0.017	0.007	175	250

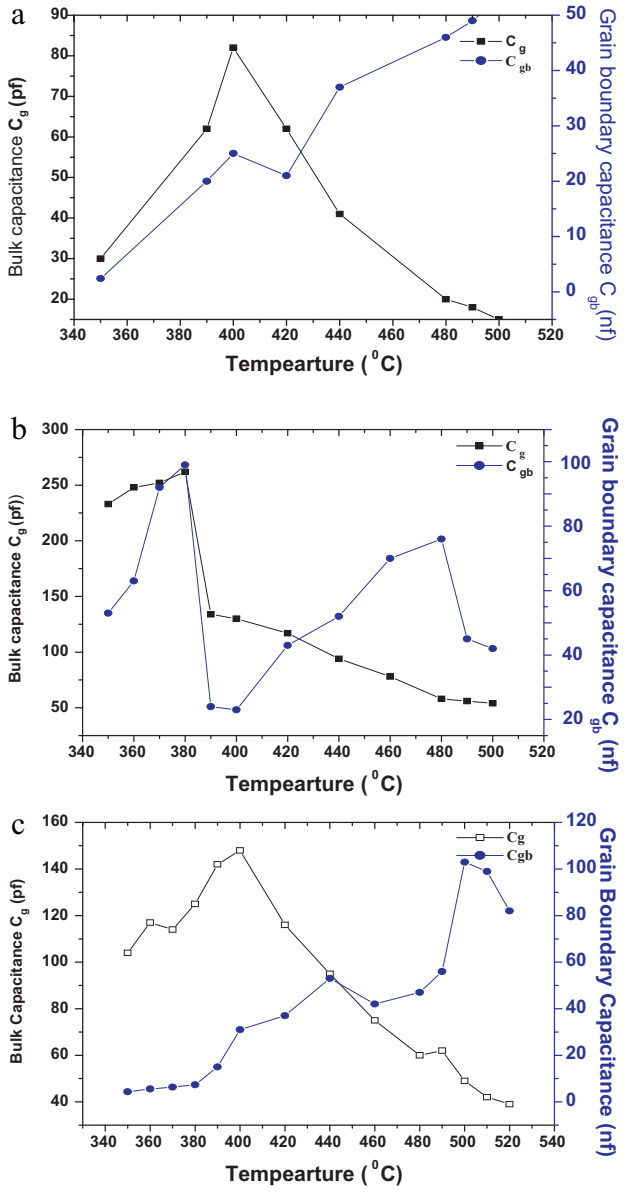

Fig. 6. Temperature variation of calculated bulk (C_g) and grain boundary (C_{gb}) capacitance in $(100-x)$ PZT/xCeO$_2$ nanocomposites for (a) $x = 0.5$, (b) $x = 1$ and (c) $x = 2$ (lines are guide to eye only).

Coming back to impedance plots, the point of intercept of the arcs on the real axis has also been recorded to be shifting towards the origin of the complex plane plot. This shift indicates a decrease in the resistive behavior of the sample assisted possibly due to grain boundary conduction with rise in temperature.

Fig. 7 shows the variation of relaxation times $\boldsymbol{\tau_b}$ (R_gC_g) and $\boldsymbol{\tau_{gb}}$ ($R_{gb}C_{gb}$) with inverse of temperature. These plots are almost linear and obeys an Arrhenius relationship $\tau = \tau_0 \exp(E_a/k_BT)$, where E_a is the activation energy for conduction and k_B is the Boltzmann constant.

Fig. 8 shows the loss spectrum (Z'' vs. f) at different temperatures in all the fine grain nanocomposites. The curves show that the Z'' values reach a maxima for the temperatures above 350 °C. The values of Z''_{max} recorded to be shifting towards higher frequencies with a decrease in the peak height upon increasing temperature. Since the peak heights are proportional to bulk resistance (R_b) according to equation

$$Z'' = R_b\left[\frac{\omega\tau}{1+\omega^2\tau^2}\right]$$

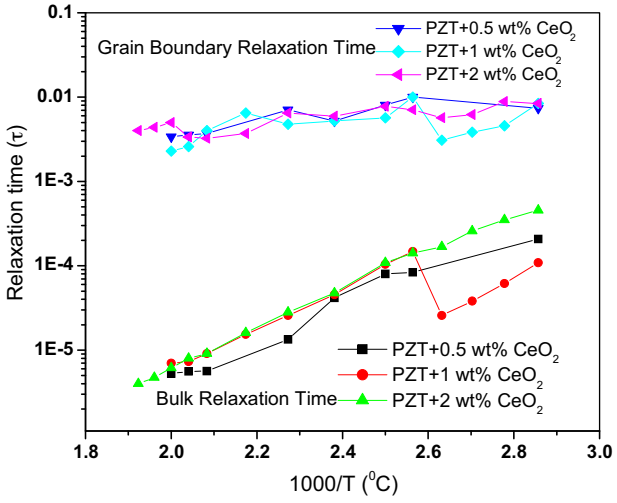

Fig. 7. Arrhenius plots of bulk and grain boundary relaxation times in $(100-x)$ PZT/xCeO$_2$ nanocomposites calculated from impedance spectra.

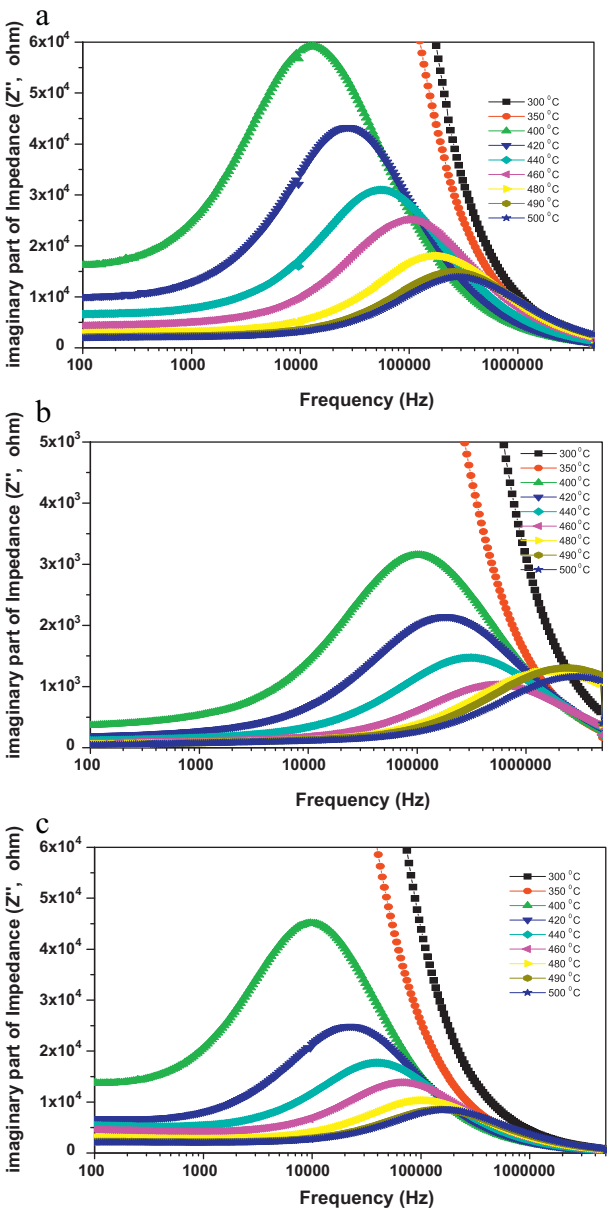

Fig. 8. Frequency variation of Z'' in $(100 - x)$ PZT/xCeO$_2$ nanocomposites for (a) $x = 0.5$, (b) $x = 1$ and (c) $x = 2$ at different temperatures.

the decrease in peak height designates a reduction in bulk resistance and therefore increased losses in the system.

It is worth noticing that, there is also a variation in peak frequency and intensity as the secondary phase weight ratio changes. Losses were found to be maximum in 1 wt% ceria added nanocomposites, since it shows highest peak frequencies with lowest intensities in comparison to other samples. As grain size decreases down to 500 nm (i.e. up to 1 wt%), ratio of grain boundary resistivity and bulk resistivity decreases (data not shown here) which tends to decreases the loss peak intensity while shifting them towards higher frequency [22]. However, the grain size reduction in 2 wt% sample is accompanied by segregation of excess ceria nanoparticles (Fig. 1(d)) in grain boundary area. Excess ceria might aid in reducing the number of charged defects [23] and led to an increase in grain boundary resistivity, thereby lowering the peak frequency and increased intensity in loss spectra.

4. Conclusions

In PZT/CeO$_2$ nanocomposites, capping of PZT grains by ceria resulted in to a fine grain microstructure with a narrow size distribution. Sintering temperature is also reduced by 200 °C on addition of ceria nanoparticles. Capping induces strain in the lattice and does not let the structure to lose its tetragonality, which normally happens when grain size reaches submicron range. In addition to this, calculated tetragonality (c/a) is found to be directly related to the average particle size rather than grain size variation in PZT-ceria nanocomposites.

Frequency-temperature dependence of imaginary part of impedance provided an in-depth knowledge about the grain and grain boundary activation in the composite system. An enormous change in impedance spectra (Z' vs. Z'') at temperatures above 350 °C signify the onset of grain boundary phase contribution to the dielectric properties of the nanocomposites. Both bulk and grain boundary relaxation processes follows Arrhenius law in fine grain nanocomposites.

Acknowledgements

Authors would like to thank Prof. R.C. Budhani, Director National Physical Laboratory, New Delhi, for his continuous encouragement and interest in this work. We also would like to thank Dr. K.N. Sood for SEM characterizations. One of the authors (Puja Goel) would like to thank Department of Science and Technology for providing a research grant under WOS-A Scheme.

References

[1] J.F. Scott, Ferroelectric Memories, Berlin, Springer, 2000.
[2] G.H. Haertling, Ferroelectric ceramics: history and technology, J. Am. Ceram. Soc. 82 (4) (1999) 797–818.
[3] Y. Xu, Ferroelectric Materials and Their Applications, Elsevier Science Publisher, The Netherlands, 1991.
[4] K. Ishikawa, K. Yoshikawa, N. Okada, Size effect on the ferroelectric phase transition in PbTiO$_3$ ultrafine particles, Phys. Rev. B 137 (10) (1988) 5852–5856.
[5] I. Ivan, L. Naumov, Bellaiche, Fu Naumov, Unusual phase transitions in ferroelectric nanodisks and nanorods, Nature 432 (2004) 737–740.
[6] M. Venkata Ramana, M. Penchal Reddy, N. Ramamanohar Reddy, K.V. Siva Kumar, V.R.K. Murthy, B.S. Murty, Nanocrystalline Pb(Zr$_{0.52}$Ti$_{0.48}$)O$_3$ ferroelectric ceramics: mechanical and electrical properties, J. Nanomater. (2010) 1–8.
[7] H.T. Chunga, D.S. Cheongb, C.S. Kim, Role of nanoparticle in PNN-PZT/Ag nanocomposite, Mater. Lett. 59 (2005) 920–924.
[8] C. Puchmark, G. Rujijanagul, S. Jiansirisomboon, T. Tunkasiri, N. Vittayakorn, T. Comyn, et al., Mechanical property evaluation of PZT/Al$_2$O$_3$ composites prepared by a simple solid-state mixed oxide Method, Curr. Appl. Phys. 6 (2006) 323–326.
[9] K. Tajima, H.J. Hwang, M. Sandob, K. Niiharac, PZT nanocomposites reinforced by small amount of oxides, J. Eur. Ceram. Soc. 19 (1999) 1179–1182.

[10] P.Goel, K.L. Yadav, A comparative analysis of PBZT synthesized by co-precipitation and sol–gel method, Ind. J. Eng. Mater. Sci. 12 (2005) 552–556.
[11] A.L. Patterson, The Scherrer formula for X-ray particle size determination, Phys. Rev. 56 (1939) 978–982.
[12] H.A. Esfahani, M.R. Vaezi, L. Nikzad, B. Yazdani, S.K. Sadrnezhaad, Influence of SiC nanoparticles and saccharin on the structure and properties of electrodeposited Ni–Fe/SiC nanocomposite coatings, J. Alloys Comp. 484 (2009) 540–544.
[13] Uta Helbig, Size effect in low grain size neodymium doped PZT ceramics, J. Eur. Ceram. Soc. 27 (2007) 2567–2576.
[14] Z. Zhao, V. Buscaglia, M. Viviani, M.T. Buscaglia, L. Mitoseriu, A. Testino, et al., grain size effect on the ferroelectric behavior of dense nanocrystalline $BaTiO_3$ ceramics, Phy. Rev. B 70 (2004) 1–5.
[15] B. Tiwari, R.N.P. Choudhary, Study of impedance parameters of Ce modified $Pb(Zr_{0.65-x}Ce_xTi_{0.35})O_3$ ceramics, IEEE Trans. Diele. Elec. Inst. 17 (2010) 5–17.
[16] K.S. Cole, R.H. Cole, Dispersion and absorption in dielectrics. Alternating current characteristics, J. Chem. Phys. 9 (1941) 341–351.
[17] J. Liu, C.G. Duan, W.G. Yin, W.N. Mei, R.W. Smith, J.R. Hardy, Large dielectric constant and Maxwell–Wagner relaxation of $Bi_{2/3}Cu_3Ti_4O_{12}$, Phys. Rev. B 70 (1–7) (2004) 144106.
[18] J.R. Macdonald, Impedance Spectroscopy Emphasizing Solid Materials and Systems, Wiley, New York, 1987 (Chapter 4).
[19] D.C. Sinclair, A.R. West, Impedance and modulus spectroscopy of semiconducting $BaTiO_3$ showing positive temperature coefficient of resistance, J. Appl. Phys. 66 (1989) 3850–3856.
[20] A.K. Jonscher, The 'universal' dielectric response, Nature 267 (1977) 673–679.
[21] P. Khatri, B. Behera, V. Srinivas, R.N.P. Choudhary, Complex impedance spectroscopic properties of $Ba_3V_2O_8$ ceramics, Res. Lett. Mater. Sci. 2008 (2008) 5.
[22] S. Chao, V. Petrovsky, F. Dogan, Complex impedance study of fine and coarse grain TiO_2 ceramics, J. Amer. Ceram. Soc. 93 (10) (2010) 3031–3034.
[23] N. Umezawa, Effects of capping HfO_2 with multivalent oxides toward reducing the number of charged defects, Appl. Phys. Lett. 96 (2010) 162906, pp3.